# Insights from underwater high resolution dissolved methane sensing over a known methane seepage site west of Svalbard

**Jack triest[1*], Pär Jansson[2*], Roberto Grilli[1], Bénédicte Ferré[2], Anna Silyakova[2], Jürgen Mienert[2], Jérôme Chappelaz[1]**

[1] Institute of Geoscience and Environment, Université Grenoble Alpes, CNRS, F-38000 Grenoble, France
[2] CAGE-Center for Arctic Gas Hydrate, Environment, and Climate, Department of Geosciences, UiT-The Arctic University of Norway, 9037 Norway.

* Corresponding authors: Jack Triest (Subocean2015@gmail.com), Pär Jansson (per.g.jansson@uit.no)

Key Points:

- A new fast-response membrane inlet laser spectrometer sensor provided high-resolution measurements of dissolved $CH_4$ offshore Svalbard near intensive bubble seepage
- Towed instrument profiles uncovered both horizontal and vertical $CH_4$ structure with unprecedented details, highlighting the need for high-resolution sensing for accurate $CH_4$ inventories and flux estimates
- New control volume and 2-dimensional models, based on seepage locations and flow rates, reproduced the high-resolution observations

**Abstract**

Methane ($CH_4$) in marine sediments have the potential to contribute to changes in the ocean- and climate system. The distribution of dissolved $CH_4$ in the oceans and lakes is influenced by physical and biochemical processes that are difficult to quantify with current standard methods such as acoustic surveys and discrete sampling. Detailed observations of subsea $CH_4$ concentrations are required to better understand the $CH_4$ dynamics in the water column, which effects ocean acidification, chemosynthetic ecosystems and the atmospheric gas composition. Here we present high-resolution in-situ measurements of dissolved $CH_4$ throughout the water column at a 400 m deep $CH_4$ seepage area west of Svalbard, obtained with a new fast-response membrane-inlet laser spectrometer sensor. We observe decameter-scale variations of dissolved $CH_4$ concentrations over the $CH_4$ seepage zone, well reproduced with a numerical model based on acoustically detected free gas emissions from the seafloor, whereas previous studies could not resolve the variability and assumed smoother distributions. We show good repeatability of the measurements by the instrument, which are also in agreement with discrete sampling. We identify sources of $CH_4$, not detected by echosounder, and rapid dispersion of dissolved $CH_4$ away from the sources. Results from this unique continuous data have and modelling efforts have a significant impact on the understanding of $CH_4$ fluxes and its spatial distribution over a $CH_4$ degassing area.

**Plain Language Summary**

Methane bubbles escaping from the seafloor may, if they reach the atmosphere contribute to the global warming effect caused by greenhouse gases (gases that can trap heat in the Earth's atmosphere). Such gas bubbles are observed in, among other places, the Arctic Ocean. Using a newly developed high-resolution methane sensor near a bubble seep location west of Svalbard revealed a patchy pattern with unprecedented details. Newly constructed numerical models reproduced the high-resolution measurements and sparse water sampling with subsequent analysis using traditional methods (gas chromatography) confirmed the sensibility and accuracy of the new sensor. Previous studies have measured with course resolution, most likely wrongly estimating the amount of methane in the seawater. For the first time, methane distribution was mapped in high resolution, which brought new insights to the bubble-mediated methane dynamics in aquatic environments. We hope that the development of the new sensor and models will bring about more similar research to provide details of methane seepage in locations worldwide.

## 1 Introduction

$CH_4$ fluxes from gas bearing ocean sediments have been a matter of concern for many years (e.g. Westbrook et al., 2009; Ferré et al., 2012; Ruppel and Kessler, 2016). Warming of bottom waters, geological triggering and local glacier state development could, at different time scales, lead to $CH_4$ gas release from the seabed. The magnitude and trend of such a phenomenon is still under debate (e.g. Hong et al., 2018; Ruppel and Kessler, 2016; Andreassen et al., 2017). Once released and dissolved in the water column, the $CH_4$ gas diffuses and is partly oxidized in the water column (Reeburgh, 2007), contributing to the ocean acidification (Biastoch et al., 2011) and minimum oxygen zones formation (Boetius and Wenzhöfer, 2013). At shallow seepage sites, $CH_4$ could ultimately reach the atmosphere and amplify greenhouse warming (Shakhova et al., 2010; Shakhova et al., 2014)
Most previous studies of $CH_4$ fluxes and distribution in the water column over hydrate-rich sediments relied on indirect or discrete sample (DS) measurements (Damm et al., 2005; Westbrook et al., 2009;

Gentz et al., 2014). Using hydro-acoustic imaging and additional bubble catcher, the bubble size and rising speed are used to derive $CH_4$ flow rates (Sahling et al., 2014; Weber et al., 2014; Veloso et al., 2015). This indirect method can only quantify the $CH_4$ flux from acoustically detectable or visible bubbles. It cannot detect $CH_4$ from sources other than free gas seepage and does not provide details on the distribution of dissolved $CH_4$ in the water column. Using this method, Sahling et al. (2014) estimated an average flowrate of 56.7 l $min^{-1}$ using this method in the area of the present study. The authors assumed that each of the 452 detected flares (the acoustic signatures of one ore many bubble streams observed in echograms) were composed of six bubble streams with an average flow rate of 20,9 ml $min^{-1}$, and compared it to previous studies (Reagan Matthew et al., 2011; Westbrook et al., 2009; Marín-Moreno et al., 2013; Berndt et al., 2014).
Discrete sampling with Niskin bottles allows direct measurement of the dissolved $CH_4$ but at limited spatial resolution. The same seep area has been documented with this method by Graves et al. (2015) and the low resolution led to an artificially smoothed spatial distribution and to a high estimation of average dissolved $CH_4$ concentration.

Current commercial underwater $CH_4$ sensors are mostly designed for long-term monitoring and do not have the required response time for accurate high-resolution mapping. (Gentz et al., 2014) deployed an underwater membrane inlet mass spectrometer with a fast response time for mapping of $CH_4$ in the same region but only at shallow (10 m) depths. One of their main hypotheses, that the vertical distribution of the $CH_4$ is limited due to stratification, is still based on discrete samples. Boulart et al. (2013) used an in situ, real time sensor in the Baltic Sea but it was not deployed over a comparable $CH_4$ hydrate zone and the reported instrument response time of 1 – 2 minutes and a detection limit of 3 nmol $l^{-1}$ are still limiting for fast profiling and background concentration studies linked to the atmosphere.

In this work, we present for the first time in-situ high-resolution mapping of dissolved $CH_4$ in seawater over active seepage, obtained by deploying a patent-pending membrane inlet laser spectrometer (MILS) (Triest et al. patent France No. 17 50063). The investigated area is located at 78°33´N 9°30´E, where the average water depth is ~390 m and more than 250 flares have been previously detected (e.g. Sahling et al., 2014; Westbrook et al., 2009; Damm et al., 2005; Graves et al., 2015). The new high-resolution measurements, together with echosounder data, sparse discrete water sampling and newly constructed control volume- (CV) and 2-dimensional (2D) models allow for a better understanding of $CH_4$ flux from the seabed and its subsequent fate in the surrounding water.

The hydrography of the area is mainly controlled by the northward flowing West Spitsbergen Current (WSC), which transports Atlantic Water (AW, S>34,9 PSU, T>3° C) (Schauer et al., 2004). The East Spitsbergen Current (ESC), flows south-westward from the East Spitsbergen coast, and northward along the western Svalbard margin, carrying Arctic Surface Water (ASW, $34.4 \leqslant S \leqslant 34.9$ PSU) and Polar Water (PW, S<34.4 PSU) above the Atlantic Water (Skogseth et al., 2005) via the Coastal Current (CC) (Loeng, 1991; Skogseth et al., 2005). The lower Arctic Intermediate Water (LAIW, S>34.90‰, $T \leqslant 3$ °C) flows below the Atlantic Water.

## 2 Materials and Methods

The survey was performed with RV Helmer Hanssen in October 2015 (CAGE 15-6 field campaign) over a well-documented area of active $CH_4$ venting (Damm et al., 2005; Westbrook et al., 2009; Sahling et al., 2014) west of Prins Karls Forland, Svalbard (Figure 1a) in 2015. Over a period of three

days (October 21 – 23), water column data was collected over an area of ~18 $km^2$ with a water depth of ~ 350 – 420 m.

## 2.1 Hydrocasts with discrete water sampling

Vertical profiles of seawater salinity, temperature and pressure were recorded at 10 stations (Figure 1.) using a SBE 911 plus CTD (Conductivity, Temperature, Salinity) probe mounted on a rosette, which also carried 12 Niskin bottles of 5 litres. The Niskin bottles were closed during the up-casts collecting seawater at different depths for following analysis. Gas chromatography (GC) analysis for CH4 concentrations was carried out in the laboratory at the Department of Geoscience, The Arctic University of Norway in Tromsø. The operated GC, a ThermoScientific Trace 1310, was equipped with a FID and a ThermoScientific TG-Bond Msieve 5A column. Hydrogen was used as the carrier gas with a flow of 10 ml/min. The temperature of the oven was a constant 150°C. Calibration of the setup was performed using three standards with known mixing ratios of 1.8, 19 and 1800 ppm $CH_4$. The instrument precision was estimated to 4%, based on the standard deviation of replicate samples. The resulting headspace mixing ratios (ppmv) were converted to in-situ concentrations (nmol $l^{-1}$), taking into account dilution of the samples from addition of reaction stopper (1 ml of 1M NaOH solution), and removal of sample water while introducing headspace gas (5 ml of pure $N_2$).

## 2.2 High-resolution $CH_4$ sensing

The MILS was towed each of the survey days, collecting in-situ data during a total of 28 hours with a sampling rate of 1 $s^{-1}$. The instrument was lowered and heaved in the water for vertical casts and towed along lines with varying heights above the seabed. The five lines closest (~15 m) to the seafloor are shown in figure 1.

The battery-powered sensor (Figure 1b) has an inlet system with a polydimethylsiloxane membrane, linked to an optical feedback cavity-enhanced absorption spectrometer (OFCEAS) and an integrated PC for control and data storage. SHDSL-communication over an 11 mm Norddeutsche Seekabelwerke CB7000 coaxial winch cable enabled real-time instrument control and data monitoring from the vessel, allowing instant decision-making and ensuring optimal sensor operation. This proved particularly useful to maintain a consistent distance from the seafloor while towing by monitoring the pressure and controlling the winch cable payout.

Sensors with membrane inlets can be sensitive to fluctuating water flow over the membrane, which can result in artificial variability of measured concentrations. This has been avoided by careful positioning of the Sea-Bird SBE5T water pump to minimize inlet/outlet pressure changes and subsequent flow variations.

The MILS was towed together with an Aanderaa, Seaguard TD262a CTD, providing temperature, salinity and dissolved oxygen data as well as pressure.

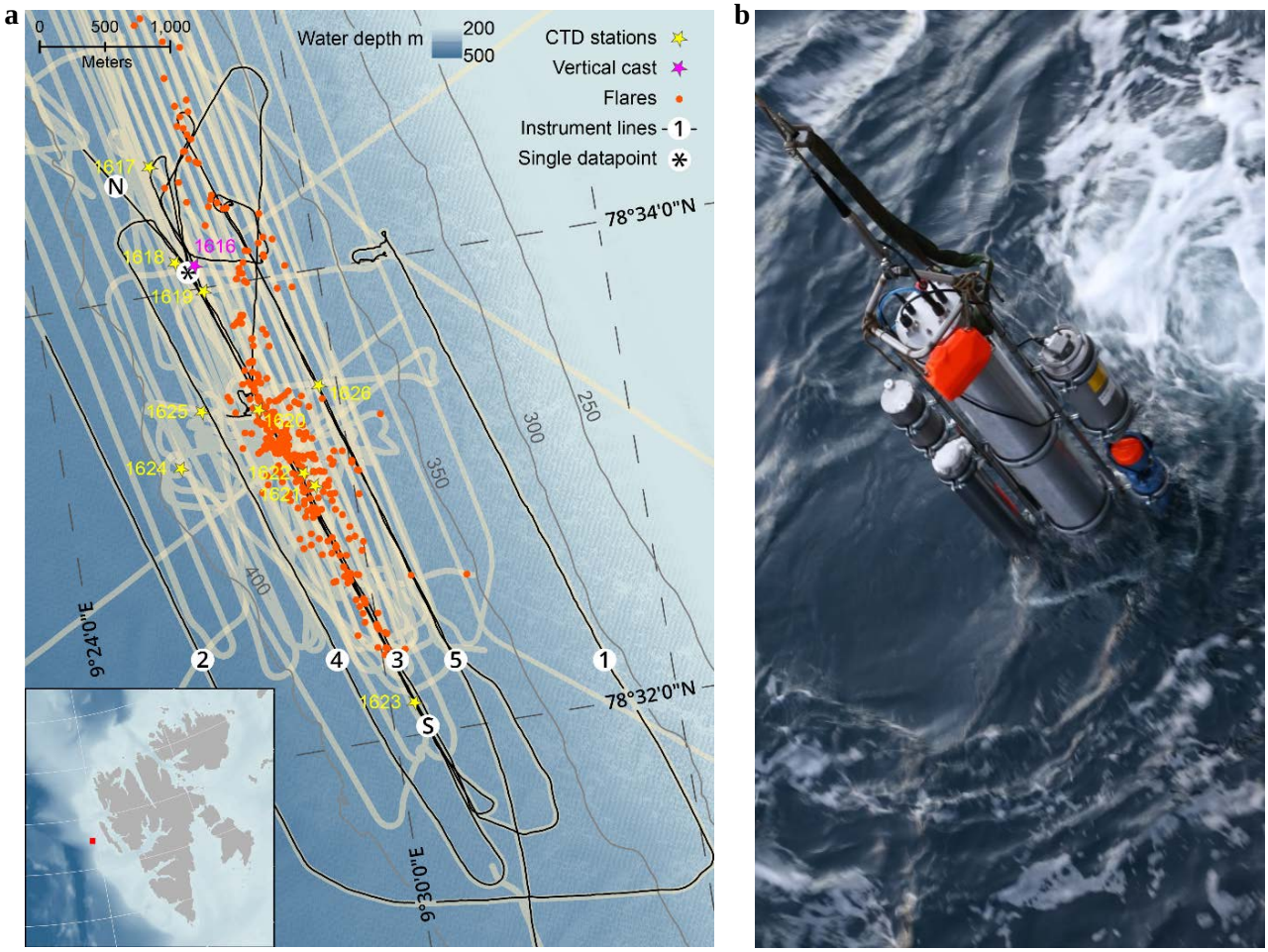


**Figure 1.** Map of the surveyed area and instrument assembly. **a)** Survey lines and sampling locations over the study area at the Svalbard continental margin. Black lines show the ship trajectory with line numbers assigned in the order they were surveyed. Beige areas (appearing as thick lines) indicate echo sounder beam coverage from this campaign and previous cruises (2010, 2013). The start- and end-locations of line 3 are indicated with N and S respectively and the black asterisk indicates the position of the data point along line 3, used for comparison with discrete samples and vertical cast. Known flare locations from this survey and CAGE-surveys in 2010 and 2013 are marked by orange dots. Discrete sampling/CTD stations are marked with yellow stars and the vertical instrument cast with a purple star. The inset image shows an overview of Svalbard with the survey location indicated with a red square. **b)** Instrument assembly. The main central tube is the prototype MILS sensor. The stainless steel frame acts as a stable platform and allows attachment of instrument battery (top right side), CTD (blue at the bottom right) and a commercial $CH_4$ sensor and its battery pack.

A stainless steel frame attached to the winch cable served as a platform to which instruments and battery (STR Seacell NiMH, 36Ah, 26VDC, 12 hours autonomy) were attached. Total height of the assembly was ~1.4 m with a total weight in air of ~160 kg and a negative buoyancy of ~52 kg. All the parameters from the MILS sensor, including gas flow, pressure, sample humidity, and internal temperature were logged to process and evaluate the $CH_4$ data. A dedicated ship mounted GPS was used to log positional data for accurate synchronization of the towed instrument data with ship position.

A position correction, essential for correct interpretation of data, was applied to the towed instrument data, accounting for the lag between the probe and the ship. We simulated a towing scenario (Dewey, 1999), using the instrument assembly, namely a 1.68 m long cylinder with 0.28 m diameter and a negative buoyancy of 52 kg. From the simulation, a speed-factor equation ($y = -0.2211x^5 + 1.355x^4 - 3.0126x^3 + 2.6741x^2 - 0.1609x$) was derived to account for the combined ship- and water current velocities ($x$). The distance of the probe behind the ship, and the corresponding required time-shift, was calculated by multiplying the speed-factor ($y$) by the instrument depth at each data point. This approach allows for a dynamic correction of the data positions accounting for towing with or against the current, and a near-stationary ship during vertical profiling. Correction for tidal currents was neglected since tides constituted less than 1 cm $s^{-1}$ during our deployments according to the tide model TPXO (Egbert and Erofeeva, 2002).

The water pump inlet has a fine mesh filter and a shield to avoid entry of free gas bubbles and possible subsequent artefacts resulting from gas bubbles entering the water sampling unit and reaching the membrane surface.

We converted MILS measured mixing ratios (ppmv) into aqueous concentrations (nmol $l^{-1}$) by accounting for fugacity, in-situ temperature, salinity, water vapor, and using the solubility coefficients determined by Wiesenburg and Guinasso Jr (1979).

### 2.3 Acoustic mapping and quantification of benthic $CH_4$ emissions

Gas bubbles in the water column are efficient sound scatterers and scientific echosounders can therefore be used for identifying and quantifying gas emissions. (Weber et al., 2014; Veloso et al., 2015). The target strength (TS), being the 10-base logarithmic measurements of acoustic cross sections, reveal the existence of objects in the water column. High TS values indicate high abundance of sound-scattering objects and collected time series of TS are seen in so-called echograms. Acoustic backscatter was continuously acquired from the 38 kHz channel of the ship-mounted single beam Simrad EK-60 echosounder during the entire survey. So-called flares (bubble plumes detected in the echograms) can be identified manually and distinguished from other acoustic scatterers such as fish schools, dense plankton aggregations and strong density gradients.

We used the methodology suggested by Veloso et al. (2015) and the prescribed Flarehunter software for mapping and quantifying the benthic gas release. Temperature, salinity, pressure and sound velocities are required for correct quantification and so we used water properties from the CTD-casts. The bubble size distribution observed in the study area in 2011 and 2012 (Veloso et al., 2015) was applied for the flow rate calculations, which were finally performed with the bundled Flare Flow Module. The resulting flow rates and positions were used in the mass balance calculation and in the two-dimensional model described in section 2.4 and 2.5 respectively.

### 2.4 Control volume model

The temporal evolution of a solute's concentration $C$ within a control volume $V=\Delta x \times \Delta y \times \Delta z$, oriented so that water flows through it in the x-direction can be written as:

$$\frac{dC}{dt} = \frac{Q_{IN} \times C_B}{V} - \frac{Q_{OUT} \times C}{V} + \frac{F}{V} + k\nabla^2 C \qquad (1)$$

With the following assumptions we can find an analytical solution for Equation 1: The in- and outflows ($Q_{IN}$, $Q_{OUT}$) are balanced and given by the width ($\Delta y$) and height ($\Delta z$) of the volume and a steady water current; The diffusion coefficient, $k$ is constant; The background concentration does not change; The flow, $F$ of the solute into the volume is constant.

Equation 1 can be understood as a first order differential equation and for the case of $CH_4$-bubble-emission from the seafloor, $F$ denotes the bubble flow rate into the volume. If we assume that the emitted bubble gas dissolves within the volume, and diffusion occurs across the domain (in the y-direction), the aqueous CH4 reaches the steady state concentration:

$$C_{t=\infty} = \frac{\left(\frac{Q_{IN} \times C_B}{V} + \frac{F}{V} + \frac{2k \times C_B}{(\Delta y)^2}\right)}{\frac{Q_{OUT}}{V} + \frac{2k}{(\Delta y)^2}} \quad (2)$$

### 2.5 Two-dimensional model

In order to gain insight to the physical processes behind the observed $CH_4$ variability, we constructed a two-dimensional (2D) numerical model, resolving the evolution of dissolved $CH_4$ in the water column. The model domain was made 400 m high (in the z-direction) and 4.5 km long (in the x-direction), oriented along the slope, corresponding to MILS line 3 (Figure 1). The navigation data along line 3 was linearly interpolated, to form the basis for a 1-meter gridded model domain starting at 78°34.54'N 9°25.92'E and ending at 78°32.1'N 9°30.58'E as indicated by N and S, in Figure 1. Flarehunter derived flow rates within 50 m from line 3 were projected onto the model domain in appropriate x/z positions.

The bubble-mediated dissolved $CH_4$ sources were distributed vertically by deriving a non-dimensional dissolution-function $S0(z) = 6.6 \times 10^{-5} \times e^{-0.066 \times z}$, with $\int S0(z)\, dz = 1$, based on the detected vertical $CH_4$ distribution near bubble streams (CTD casts 1618, 1619 and 1620). Source distribution functions, *S(z)* were calculated by scaling *S0(z)* with the Flarehunter derived flow rates and distributed into current-corrected x/z nodes with volumes $\delta v = \delta x \times \delta y \times \delta z$, where δx=δz=1 m and δy is the model width.

The 2D model was run to steady state while simulating horizontal $CH_4$ diffusion across the domain and advection with water currents, similarly with the CV model.

## 3 Results

### 3.1 Water properties

The pressure- salinity and temperature measurements from both the towed CTD and vertical casts indicate that the water is well mixed in the bottommost 150 meters and continuously stratified from 250 to 50 mbsl with a squared buoyancy frequency of ~$N^2 < 4 \times 10^{-5}$ $s^{-2}$. A pycnocline was observed at 10 – 30 mbsl (Figure 2a) with $N^2$ up to $10^{-4}$ $s^{-2}$. Temperature and salinity measurements indicate that mainly AW is present below ~20 mbsl and the overlying water is intermediate (IW) and surface water (SW) as seen in Figures 2c and 2d. The temperature close to the seafloor was 4.2 – 4.4 °C, which is more than 1°C above the $CH_4$ hydrate stability zone calculated according to Tishchenko et al. (2005) with a salinity of 35.1 PSU as indicated in Figure 2a.

The velocity of the WSC was between 0.1 and 0.3 $ms^{-1}$ (Figure 2b), inferred from the inclination of flare spines (Veloso et al., 2015), which is consistent with previous findings (Graves et al., 2015; Gentz et al., 2014).

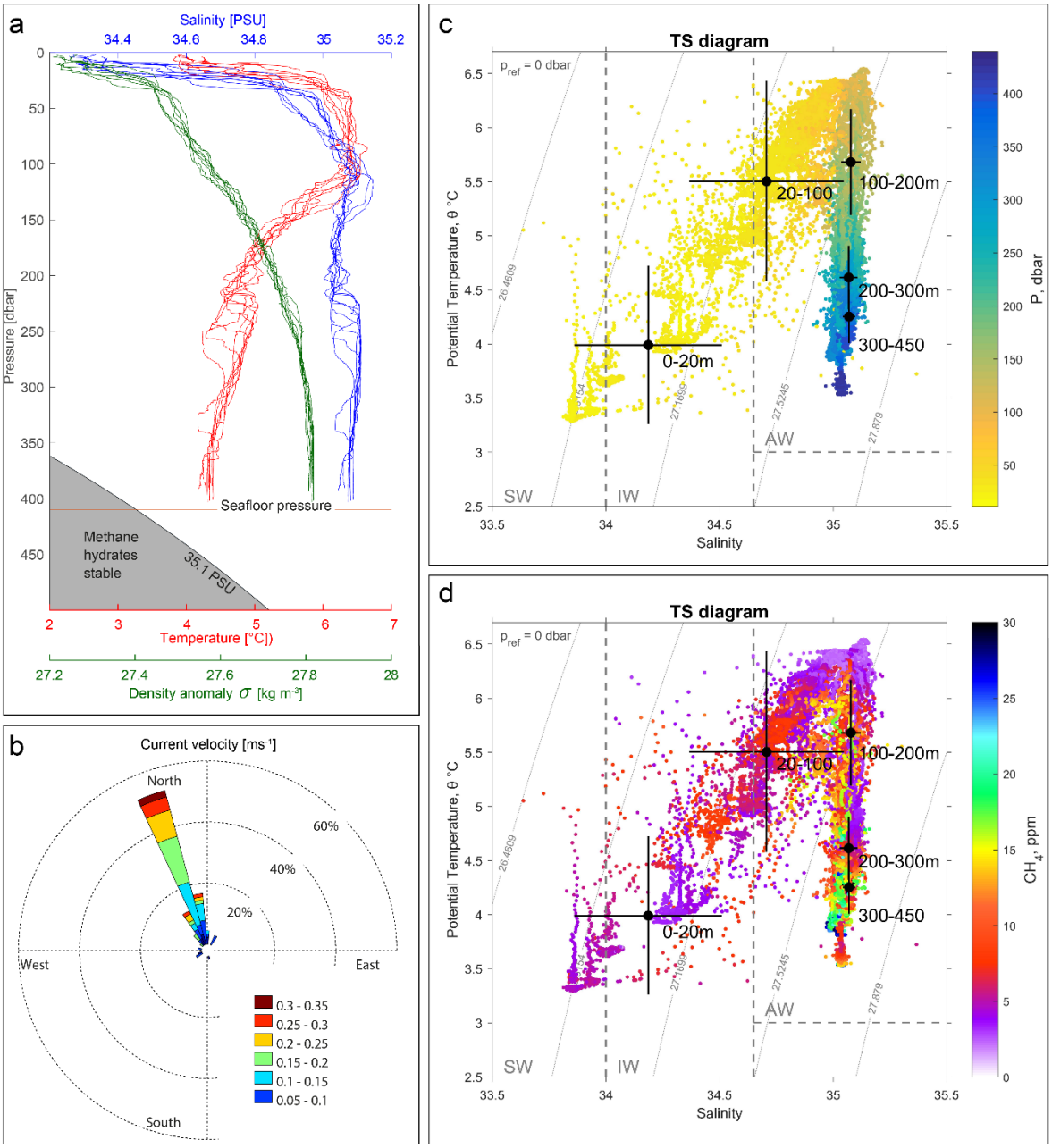


**Figure 2.** Hydrography during the campaign. **a)** CTD casts 1617- 1626 showing potential temperature (red), practical salinity (blue) and density anomaly calculated with Gibbs sweater package (McDougall and Barker, 2011) (green). **b)** Ocean currents inferred from inclination of flare spines (Veloso et al., 2015) and a mean bubble rising speed of 23 cm $s^{-1}$. **c)** Temperature and salinity diagram colored by pressure (dbar). AW indicates Atlantic Water, IW is Intermediate Water and SW is surface Water. Back dots indicate the mean water properties for layers [0 – 20, 20 – 100, 100-200, 200-300, 300-450 mbsl]. Crosses indicate the standard deviation within the corresponding layer. **d)** TS diagram colored by $CH_4$ mixing rations (ppmv) measured with the MILS. Grey curved lines in the background indicate isopycnals (constant density ($\sigma$) lines). Black dots are average temperature and salinity at water depths

0-20m, 20-100m, 100-200m, 200-300m, 300-400m. Bars indicate standard deviations of potential temperature ($\theta$) and salinity.

The mean salinity in layers [0 – 20, 20 – 100, 100 – 200, 200 – 300, 300 – 400 m] were [34.19, 34.71, 35.08, 35.07, 35.07 PSU] with standard deviations [0.32, 0.34, 0.04, 0.04, 0.03 PSU] and the corresponding potential temperatures were [3.99, 5.50, 5.68, 4.61, 4.25 °C] with standard deviations [0.73, 0.93, 0.49, 0.29, 0.25 °C] as seen in Figure 2c and 2d. Warm and saline water is present in the layer between 100 and 200 meters water depth, which we consider the core of the WSC which is normally found 50 – 150 mbsl (e.g. Saloranta and Svendsen, 2001). The exact depth of the core varies with oceanographic factors with season and with mesoscale variability on weekly time scales and atmospheric forcing.

Dashed lines in Figures 2c and 2d indicate water masses according to classification by Cottier et al. (2005). This data suggest a clear dominance of Atlantic Water (AW) with T>3°C and S>34.65 during the survey. However, one should keep in mind a possible bias, since most of the data was collected at the depth of the core of the WSC.

### 3.2 Measured and modeled $CH_4$ distribution

The high-resolution dissolved $CH_4$ concentration profiles resulting from towing the MILS along five lines approximately 15 m above the seafloor show high variability (Figure 3), especially over line 3, which geographically matches the main distribution of bubble plumes (Figure 1). On the landward side (line 1 and 5), the concentration is relatively smooth, but considerably elevated (background $CH_4$ concentration of ~ 30 nmol $l^{-1}$). On the offshore side (line 2 and 4), the average concentrations are lower (~ 15 and 10 nmol $l^{-1}$) but we observe elevated $CH_4$ without hydroacoustic evidence of sources.

The down- and upward sequences obtained from the vertical MILS cast at station 1616 (Figure 1), which was recorded during 25 minutes shows excellent repeatability after accounting for the instrument lag time (corresponding to the gas flushing from the membrane to the cell) of 15 seconds (Figure 4). The sensor shows no memory effects following elevated concentrations, which are typical for other membrane-based sensors. In addition, despite spatial and temporal variations, comparison with discrete measurements from a nearby CTD cast taken a few hours later, confirms the qualitative match of the MILs measured $CH_4$ concentrations. The apparent discrepancy between the MILS data and the discrete measurements below 350 m depth is due to a slight difference in sampling location. The discrete data from station 1619 and MILS data from line 3 at the same location (asterisk in figure 4) matches extraordinarily well, supporting the qualitative match between the methods and confirms the significant spatial variability of the dissolved $CH_4$. An exponential function was fitted to the entire dataset (shown as a dotted line in figure 4) and was nondimensionalized for inclusion in the 2D model. Comparison of the MILS technique against discrete sampling has been conducted in the laboratory and will be reported in a separate publication.

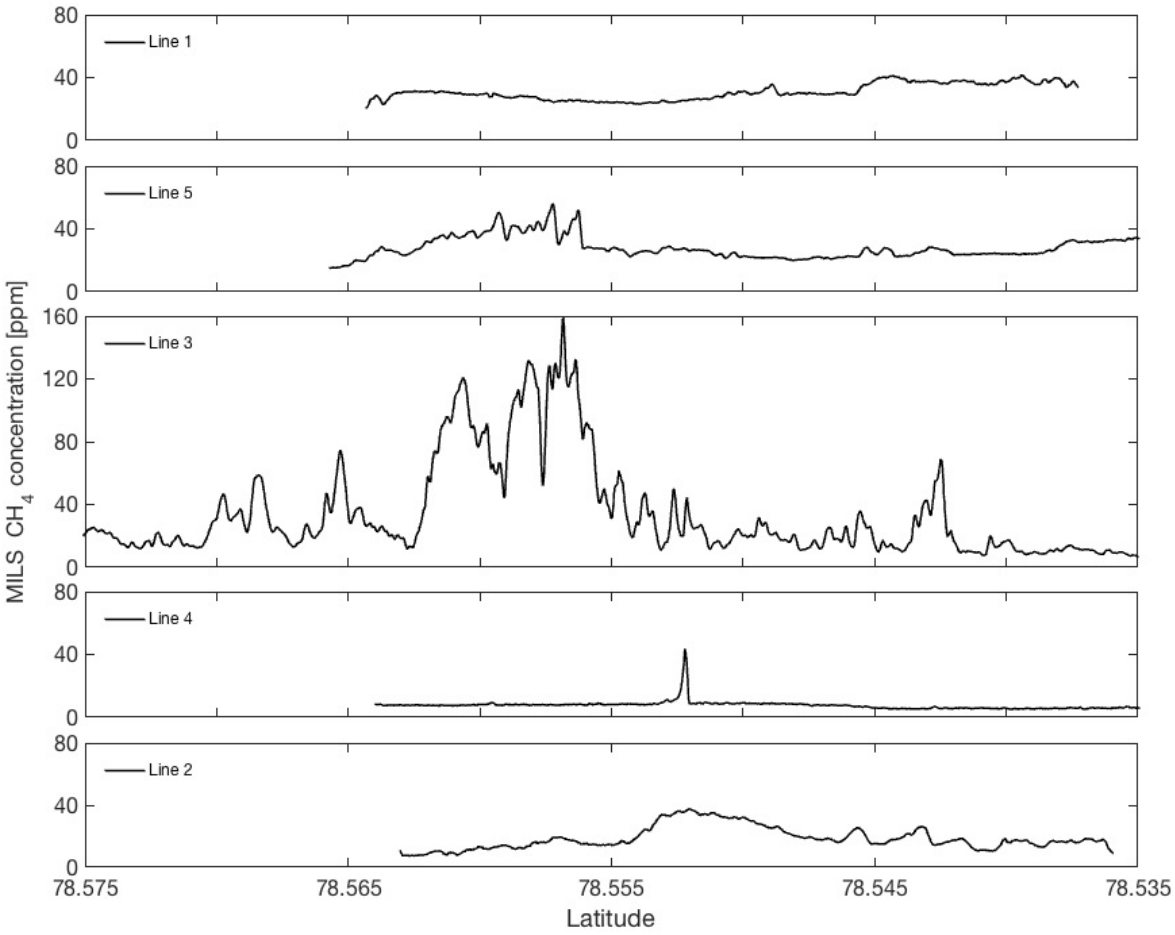


**Figure 3.** Dissolved CH4 concentrations along trajectories. The panels show data acquired with the towed MILS along lines 1 – 5, shown in order of proximity to the shore with line 1 closest to the shore and line 2 furthest offshore. Figure 1a shows the horizontal trajectories of the lines.

Elevated concentrations peaking at ~160 and ~220 mbsl revealed by the continuous vertical profiling was not identified with the discrete sampling in either of the nearby CTD stations (1618 and 1619) because of the sparse sampling (Figure 4). The MILS data collected 15 meters above seafloor along line 3 and near the vertical MILS-cast (1616), does not reveal the high concentrations (~200 nmol/L) measured during the vertical profiling, emphasizing the temporal variability of the $CH_4$ distribution.

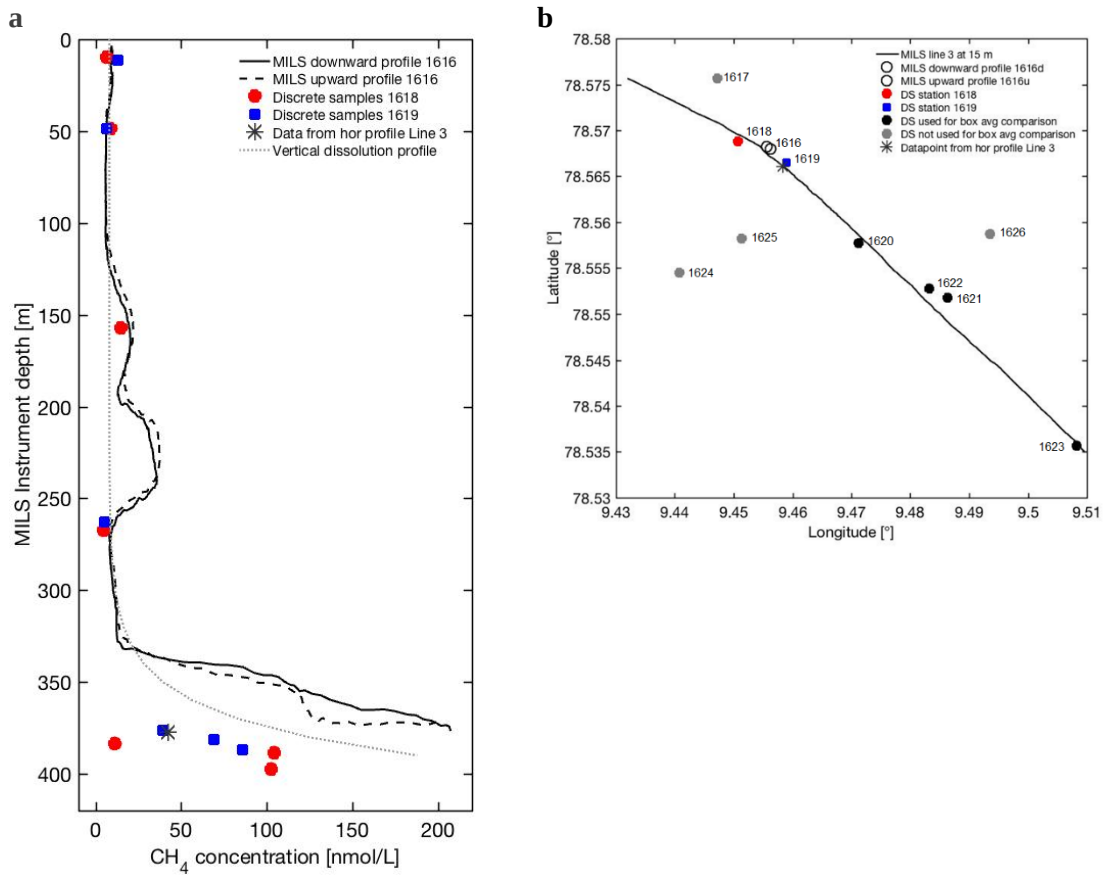


**Figure 4.** Vertical high-resolution $CH_4$ profiles and discrete samples. **a)** The solid and dashed black lines represent the continuous downward and upward profiles after correction for instrument response time. Discrete sample data is shown as red dots and blue squares for comparison. The black star indicates the data point from the continuous horizontal profile along line 3, closest to the vertical cast 1616. The dotted line indicates an exponential function fitted to the $CH_4$ concentrations of the discrete samples. **b)** Location of discrete sampling stations and vertical profile positions in relation to the horizontal profile of line3 (black line).

We observe high $CH_4$ variability in the horizontal profiles (Figure 3). Hence, we focus on a trajectory (line 3, towed in north-south direction at ~0.8 m $s^{-1}$) directly over the flares for further analysis. The fast response time of the MILS sensor ($T_{90}$<30 secs) revealed decameter-scale variations of the dissolved $CH_4$ concentrations with high values well correlated with the echo-sounder signal (Figure 5) after correcting for the towed instrument position.

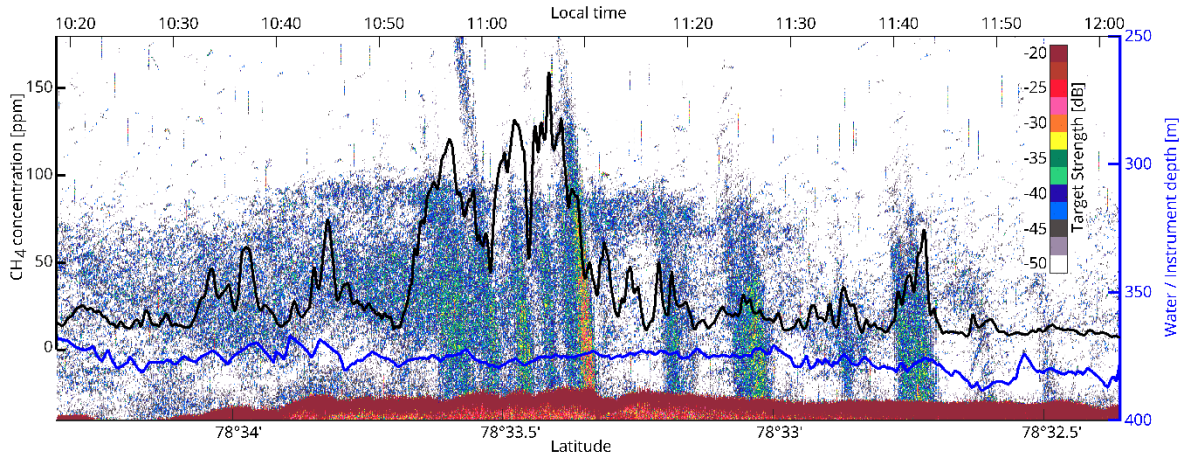


**Figure 5.** Towed MILS data overlying echo sounder data. The black line shows the $CH_4$ concentration along line no. 3 (see Fig. 1 for location) at ~15 m from the seafloor. The blue line indicates the depth of the towed instruments. The echogram displaying TS (color bar) values from the 38 kHz channel is shown in the background. Brown and red indicates strong backscattering, seen at the seafloor and in some of the most intense flares.

Correlations of $CH_4$ concentrations versus depth and speed changes were low (R= 0.0133, -0.0001, -0.0094, 0.0028 for ship speed, ship acceleration, vertical instrument speed and instrument acceleration respectively), showing the stability of the instrument during rapid movements and no effect from fluctuating flow over the membrane was detected.

Methane sources forcing the CV- and 2D model were obtained from the acoustic mapping and quantification described in section 2.3. During the entire survey, we identified 68 unique (107 before clustering) bubble plumes (flares in the echograms) emissions with an average flow rate of 192 ml $min^{-1}$ and a standard deviation of 198 ml $min^{-1}$. In close vicinity of line 3, 31 bubble streams were identified, with an average flow rate of 240 ml $min^{-1}$ (s.d. 261 ml $min^{-1}$) amounting to 7.44 l $min^{-1}$.

These flow rates were taken as sources in both the CV- and the 2D model, but since the flow rates were calculated in a layer 5 – 10 m above the seafloor, they were upscaled by 40% to compensate for bubble dissolution near the seafloor.

The dimensions of the models were chosen to match line 3, which has a length of ~4.5 km. A height of 75 m was chosen for the control volume, since we assume that the bulk of the emitted $CH_4$ dissolves within this distance from the seafloor. The 2D model resolved the full height of the water column (400 m) and the width of both models were set to 50 meters.

The 2D model was run to steady state with different diffusion coefficients, $k \in [0.3 - 4.9\ m^2\ s^{-1}]$, which were adopted from dye-experiment results in the shelf sea offshore Rhode Island (Sundermeyer and Ledwell, 2001). Results revealed that the best fit (R=0.81) was achieved during a simulation with $k$=1.5 $m^2s^{-1}$ which reached steady state after ~1 hour. The resulting range of model outputs and the best fit-model simulation are visualized in Figure 5.

Applying the same diffusion coefficient in the CV model resulted in a steady state concentration of 23.5 nmol $l^{-1}$ (23.2 nmol $l^{-1}$ was reached in 53 min).

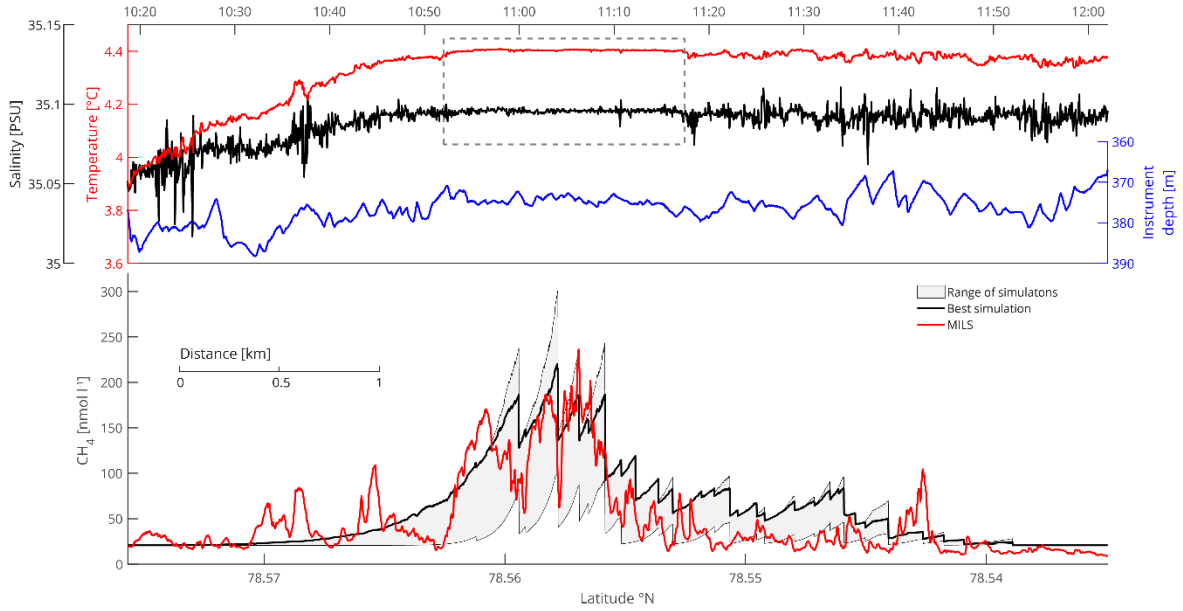


**Figure 6.** Water properties and qualitative comparison between modelled and measured dissolved CH4 concentrations. Top panel shows temperature and salinity data together with the depth of the towed instruments. The dashed-line box highlights the area of intense mixing. In the lower panel, the red line shows the dissolved $CH_4$ measured by the MILS. The grey area indicates the range of $CH_4$ concentrations from the model simulations. The black line depicts the model simulation run with the best fit (R=0.81) to the measured data.

The measured continuous profile along line 3, together with the range of 2D model outputs and the best-fit simulation ($k$=1.5 $m^2$s-1) are seen in Figure 6. Despite applying a high diffusivity, the model always shows a residual downstream tailing, not evident in the measured data, which we attribute to the fact that the model accounts for diffusion across, but not along the model domain.

The inferred high diffusion is supported by the salinity and temperature profiles of the towed CTD, which indicate well-mixed water due to intense mixing, particularly over the most prominent gas flares. Here, the standard deviation of the temperature and salinity drops by a factor of four (dashed line box in Figure 6) compared to the rest of the data.

### 3.6 Methane inventory using different methods

In order to evaluate how different methods may influence CH4 inventory calculations, we applied different methods on the same geometry.

We defined a virtual control volume (here called “box”) along the slope, which was 4500 m long and equivalent to the MILS tow line no. 3. A width of 50 m was chosen to match the echosounder beam width and limit uncertainties of contributions from neighboring bubble plumes. The height was limited to 75 m above the seabed as this is the most dynamic and $CH_4$ enriched zone and similar to the typical bubble rise height. Thus, the geometry of the “box” was 4500×50×75 m.

Data from different heights above the seafloor were used as foundations for the different calculations. Continuous horizontal profiles based on discrete samples were constructed by linear interpolation between samples from similar depths, i.e. samples from ~5, ~15 and ~20 m from the seafloor (Figure

7). Vertical gradients matching the dissolution function were applied to the horizontally interpolated data in order to arrive at vertical distributions along the horizontal. A horizontal gradient, across the width of the box, of 1.5 nmol $l^{-1}$ $m^{-1}$ was used to account for turbulent dispersion. Integration of the data and subsequent scaling by the box geometry gave the average concentrations (nmol $l^{-1}$). The method was repeated for 5, 15 and 20 m based data and results are reported as "box" values in Table 1.

The line-average concentration from the 2D model was calculated from depths following the MILS trajectory and the 2D model box-average was extracted from 390 – 315 m water depth (the 2D model is 400 m deep along the entire box). The CV model yielded one value for the entire line/box.

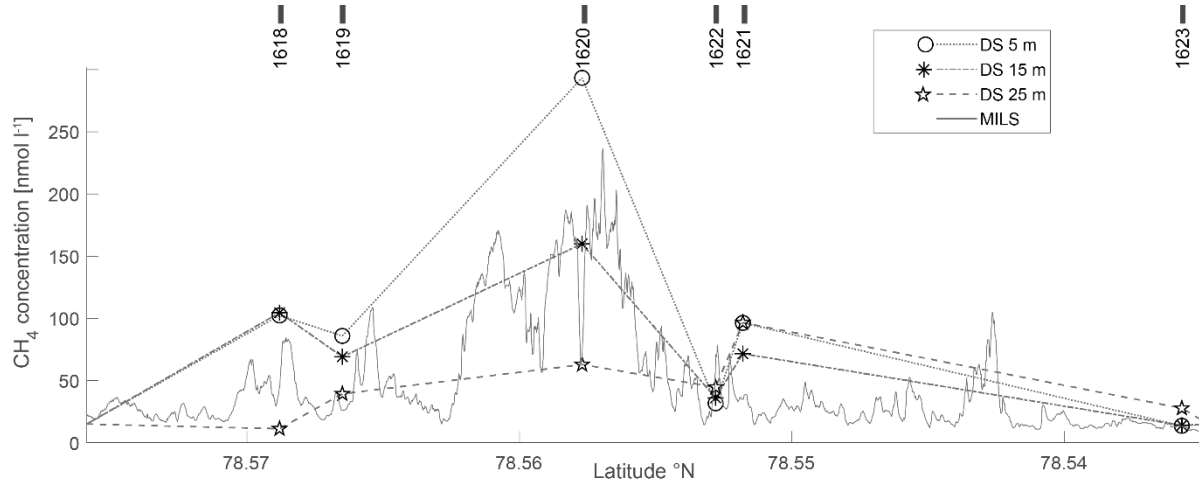


**Figure 7.** Continuous MILS profile along line 3 compared to discrete samples concentrations at various depths. Simple line averages were calculated along the box, considering either high-resolution measurements, model results or values linearly interpolated between discrete points. These results are denoted "line" in Table 1.

Despite high flow rates and additional CH4 from an unknown source, the average $CH_4$ concentration in the box volume, based on continuous data, is essentially the same as the average obtained from discrete data acquired 15 m above the seafloor (27 vs 29 nmol $l^{-1}$), while the numerical models yield slightly lower averages (19 and 20 nmol $l^{-1}$). The initial $CH_4$ box-concentration (93 nmol l-1) estimated by Graves et al. (2015) was obtained from a CTD transect across the slope and directly over the most active bubble plumes and should not be directly compared with our estimates.

**Table 1.** Average concentrations (nmol $l^{-1}$) calculated with different methods. Points indicate simple average of sparse sampling and High res. /Interpolated indicates high-resolution measurements and Interpolated values respectively.

| | | Line | | Box |
|---|---|---|---|---|
| Dataset | Meters above seafloor | Points | High resolution / Interpolated | High resolution / Interpolated |
| CV model | - | 20 | | |
| MILS | ~15 | - | 63 | 27 |
| 2D model | ~15* | - | 58 | 19 |
| DS low | ~5 | 104 | 102 | 45 |
| DS intermediate | ~15 | 76 | 71 | 29 |
| DS high | ~20 | 47 | 49 | 19 |

* Concentrations from the 2D model were extracted from depths matching the MILS instrument depth for direct comparison

## 4 Discussion

The flow rates acquired with Flarehunter agrees well with an example flow rate of 232 ml $min^{-1}$ for a single flare, using a bubble catcher (Cluster C5, Table 5 (Sahling et al., 2014)). The average flowrate obtained along line 3 (240 ml $min^{-1}$) is almost double the average of 125 ml $min^{-1}$ (6×20.9 mL $min^{-1}$) per bubble stream cluster estimated by Sahling et al. (2014). Our estimated average is higher because line 3 is directly over, and limited to, the most active venting zone in the area. The sum of the observed flow rates from 68 bubbles streams amounted to 13 l $min^{-1}$, which translates to 180 t $y^{-1}$, assuming constant flow. This may be compared to ~600 t $y^{-1}$ estimated for a bigger area by Veloso et al. (2015) and 400 t $y^{-1}$ (area 3) by Sahling et al. (2014) encompassing our area and more active seepage further north.

The MILS data collected 15 meters above seafloor along line 3 and near the vertical MILS-cast 1616 did not reveal the high concentrations (~ 200-nmol $l^{-1}$) measured during the vertical cast, emphasizing the heterogeneous $CH_4$ distribution, and the need for high-resolution sensing, rather than sparse discrete sampling.

Downstream tailing of $CH_4$ concentrations seen in the model was not observed anywhere with the MILS. In fact, a careful analysis reveal equal distribution of down-and upstream gradients. We explain the discrepancy by the fact that the model does not resolve diffusion along the model domain. If instrument response-time was a limiting factor, it would reduce both up- and downstream gradients equally and reveal any asymmetry if present. The observed symmetry suggest that $CH_4$ disperses equally in all horizontal directions around the bubble plumes while being advected away from bubble plumes. With that inference, it would be feasible to determine $CH_4$ flux from the seafloor by high-

resolution sensing during surveys designed with trajectory-spacing equal to single beam echosounder swath widths.

Enhanced $CH_4$ concentrations are mainly observed up to 75-100 meters above the seabed, which is supported by bubble models (e.g. McGinnis et al., 2006), showing that bubbles of observed sizes (~3 mm equivalent radius) transport $CH_4$ up to approximately this height. We suggest that this height limit is a result of rapid horizontal and inefficient vertical mixing. Density stratification plays an important role in the vertical distribution of $CH_4$ because considerable turbulent energy is required to mix solvents across diapycnals. Vertical mixing of solvents including $CH_4$ is therefore inhibited even without a strong pycnocline, contrary to the conception of Gentz et al. (2014), and Myhre et al. (2016), suggesting that a pycnocline is necessary as a barrier for the vertical transport.

Enhanced $CH_4$ concentrations up to 100 nmol $l^{-1}$ without the acoustic signature of flares were observed north of the active flare zone (Figure 4 and 5b). Echograms from the CAGE 15-6 survey and previous surveys (2010 and 2013) did not reveal flares in the vicinity. This may indicate one of the following: a) $CH_4$ enriched water seepage from the seafloor exist nearby, b) bubble streams with bubbles too small for detection by echosounder emanates from the seafloor, or c) $CH_4$ was advected from a nearby bubble plume source, but not along the trajectory of the instruments. In our case, a temperature- and salinity anomaly reveals mixing of AW with colder and fresher water. Because mixing lines drawn in TS diagrams point to PW rather than a fresh water source, we favor the hypothesis that the additional $CH_4$ was transported downslope with AW mixed with some PW.

The numerical model relies on mapped bubble plumes, and the difference between measured and modelled $CH_4$ is obvious from 10:30 to 10:50 in Fig 7B. The additional $CH_4$ from high-resolution data underscores that echosounder mapping and modelling is not enough to acquire a correct estimate of a $CH_4$ inventory.

Methane Concentrations peaking in midwater (~160 and 220 m) picked up by the vertical MILS cast (1616) would only by chance be picked up with discrete water sampling and could not have been inferred from echosounding, highlighting the usefulness of high-resolution $CH_4$ profiling. We did not identify the source of the elevated $CH_4$ in this location, but it may be may be attributed to nearby seepage. Known seepage locations exist only a few km away from the location at the shallow shelf (50 – 150 mbsl) and the shelf-break (~250 mbsl) (Veloso et al., 2015), but it is doubtful if seepage from these locations can reach the surveyed area, as the WSC is persistently northbound.

The continuous profile from the MILS results in a lower average concentration due to the high variability. The choice of discrete sample locations and depths can significantly affect the resulting average and highlights the consequence of low-resolution sampling and subsequent interpolation.

Even though results for the average concentrations in a specific volume can (by chance) be similar for high resolution profiling and discrete sampling, the added detail of the structure allows for better understanding of the processes that influence the dissolved gas.

## 5 Conclusion

The MILS sensor was successfully deployed from the ship while providing real-time telemetry and obtaining unprecedented details of both vertical and horizontal distribution of dissolved $CH_4$ in an area of intense seepage. Owing to the high-resolution data, we perceived more heterogeneous $CH_4$ distribution than previously presumed.

Discrete sampling with subsequent GC analysis of $CH_4$ concentrations agreed well with the MILS data while highlighting the importance of high-resolution sampling in order to resolve the variability of the $CH_4$. Average concentrations given by discrete sampling coincided, by chance, with the average from high-resolution measurements, but we showed that sparse sampling may seriously over- or underestimate averages, which may have serious consequences if the acquired concentrations are included in circulation- or climate models.

The heterogeneous distribution of the measured $CH_4$ matched with acoustic backscatter data, with very high concentrations close to the most intense flares and lower concentrations away from them. Nevertheless, we observed high concentrations also without acoustic evidence of $CH_4$ sources, even after checking additional acoustic datasets from previous surveys covering the same area. Similarly, midwater high concentrations were missed by discrete sampling during a vertical cast.

Properly accounting for the time lag between instrument- and ship observations proved essential for the data analysis, and puts forward the importance of monitoring instrument depth and cable payout during similar tow-surveys. The method could be further improved by attaching an acoustic underwater positioning device on the instrument assembly.

The high-resolution data was compared with a new 2D model, which required a high diffusion coefficient in order to reproduce the variability of measurements. This is confirmed by high turbulence in the area, understood by the strong currents.

Despite high flow rates and additional CH4 with unknown sources, the average $CH_4$ concentrations are relatively low in the area, which we attribute to fast dispersion away from the bubble plumes. The origin of the additional $CH_4$, not from local bubble plumes, remain unknown, which calls for further surveys in the area to better understand the total contribution of $CH_4$ from the area and reveal additional sources if present.

In summary, we have presented new methods for understanding the dynamics of $CH_4$ after its release from the seafloor, including a reliable and fast CH4 sensor giving high-resolution data. We employed an inverse acoustic model for seepage gas quantification, providing the basis for a new 2D forward model and a new control volume model, both in good agreement with observations. This is promising for future work of similar kind and we see many potential uses for high-resolution $CH_4$ sensing with the MILS within environmental studies and $CH_4$ sniffing, desired by the oil- and gas industry for gas leakage detection.

## 6 Acknowledgements and data

The research leading to these results has received funding from the European Community's Seventh Framework Programs ERC-2011-AdG under grant agreement n° 291062 (ERC ICE&LASERS), as well as ERC-2015-PoC under grant agreement n° 713619 (ERC OCEAN-IDs). Additional funding support was provided by SATT Linksium of Grenoble, France (maturation project SubOcean CM2015/07/18). The collaboration between CAGE and IGE was initiated thanks to the European COST Action ES902 PERGAMON. The research is part of the Centre for Arctic Gas Hydrate, Environment and Climate (CAGE) and is supported by the Research Council of Norway through its Centers of Excellence funding scheme grant No. 223259. We thank the crew on-board RV Helmer Hanssen for the assistance during the cruise, and the University of Svalbard for the logistics support. A dataset comprising the MILS sensor data and echosounder files is available from the UiT Open Research Data repository https://doi.org/10.18710/UWP6LL

## References


Andreassen, K., Hubbard, A., Winsborrow, M., Patton, H., Vadakkepuliyambatta, S., Plaza-Faverola, A., Gudlaugsson, E., Serov, P., Deryabin, A., Mattingsdal, R., Mienert, J. & Bünz, S. 2017. Massive blow-out craters formed by hydrate-controlled methane expulsion from the Arctic seafloor. *Science*, 356(6341), pp. 948-953. doi: 10.1126/science.aal4500.

Berndt, C., Feseker, T., Treude, T., Krastel, S., Liebetrau, V., Niemann, H., Bertics, V. J., Dumke, I., Dünnbier, K., Ferré, B., Graves, C., Gross, F., Hissmann, K., Hühnerbach, V., Krause, S., Lieser, K., Schauer, J. & Steinle, L. 2014. Temporal Constraints on Hydrate-Controlled Methane Seepage off Svalbard. *Science*, 343(6168), p. 284. doi: 10.1126/science.1246298.

Biastoch, A., Treude, T., Rüpke, L. H., Riebesell, U., Roth, C., Burwicz, E. B., Park, W., Latif, M., Böning, C. W. & Madec, G. 2011. Rising Arctic Ocean temperatures cause gas hydrate destabilization and ocean acidification. *Geophysical Research Letters*, 38(8). doi: 10.1029/2011GL047222.

Boetius, A. & Wenzhöfer, F. 2013. Seafloor oxygen consumption fuelled by methane from cold seeps. *Nature Geoscience*, 6(9), pp. 725-734. doi: 10.1038/ngeo1926.

Boulart, C., Prien, R., Chavagnac, V. & Dutasta, J.-P. 2013. Sensing Dissolved Methane in Aquatic Environments: An Experiment in the Central Baltic Sea Using Surface Plasmon Resonance. *Environmental Science & Technology*, 47(15), pp. 8582-8590. doi: 10.1021/es4011916.

Cottier, F., Tverberg, V., Inall, M., Svendsen, H., Nilsen, F. & Griffiths, C. 2005. Water mass modification in an Arctic fjord through cross-shelf exchange: The seasonal hydrography of Kongsfjorden, Svalbard. *Journal of Geophysical Research: Oceans*, 110(C12). doi: 10.1029/2004JC002757.

Damm, E., Mackensen, A., Budéus, G., Faber, E. & Hanfland, C. 2005. Pathways of methane in seawater: Plume spreading in an Arctic shelf environment (SW-Spitsbergen). *Continental Shelf Research*, 25(12), pp. 1453-1472. doi: 10.1016/j.csr.2005.03.003.

Dewey, R. K. 1999. Mooring Design & Dynamics—a Matlab® package for designing and analyzing oceanographic moorings. *Marine Models*, 1(1), pp. 103-157. doi: 10.1016/S1369-9350(00)00002-X.

Egbert, G. D. & Erofeeva, S. Y. 2002. Efficient Inverse Modeling of Barotropic Ocean Tides. *Journal of Atmospheric and Oceanic Technology*, 19(2), pp. 183-204. doi: 10.1175/1520-0426(2002)019<0183:EIMOBO>2.0.CO;2.

Ferré, B., Mienert, J. & Feseker, T. 2012. Ocean temperature variability for the past 60 years on the Norwegian - Svalbard margin influences gas hydrate stability on human time scales. *Journal of Geophysical Research: Oceans (1978–2012)*, 117(C10). doi: 10.1029/2012JC008300.

Gentz, T., Damm, E., Schneider von Deimling, J., Mau, S., McGinnis, D. F. & Schlüter, M. 2014. A water column study of methane around gas flares located at the West Spitsbergen continental margin. *Continental Shelf Research*, 72, pp. 107-118. doi: 10.1016/j.csr.2013.07.013.

Graves, C. A., Steinle, L., Rehder, G., Niemann, H., Connelly, D. P., Lowry, D., Fisher, R. E., Stott, A. W., Sahling, H. & James, R. H. 2015. Fluxes and fate of dissolved methane released at the seafloor at the landward limit of the gas hydrate stability zone offshore western Svalbard. *Journal of Geophysical Research: Oceans*, 120(9), pp. 6185-6201. doi: 10.1002/2015JC011084.

Hong, W. L., Torres, M. E., Portnov, A., Waage, M., Haley, B. & Lepland, A. 2018. Variations in Gas and Water Pulses at an Arctic Seep: Fluid Sources and Methane Transport. *Geophysical Research Letters*, 45(9), pp. 4153-4162. doi: 10.1029/2018GL077309.

Loeng, H. 1991. Features of the physical oceanographic conditions of the Barents Sea. *Polar Research*, 10(1), pp. 5-18. doi: 10.3402/polar.v10i1.6723.

Marín-Moreno, H., Minshull Timothy, A., Westbrook Graham, K., Sinha, B. & Sarkar, S. 2013. The response of methane hydrate beneath the seabed offshore Svalbard to ocean warming during the next three centuries. *Geophysical Research Letters*, 40(19), pp. 5159-5163. doi: 10.1002/grl.50985.

McDougall, T. J. & Barker, P. M. 2011. Getting started with TEOS-10 and the Gibbs Seawater (GSW) oceanographic toolbox. *SCOR/IAPSO WG*, 127, pp. 1-28.

McGinnis, D., Greinert, J., Artemov, Y., Beaubien, S. & Wüest, A. 2006. Fate of rising methane bubbles in stratified waters: How much methane reaches the atmosphere? *Journal of Geophysical Research: Oceans (1978–2012)*, 111(C9). doi: 10.1029/2005JC003183.

Myhre, C. L., Ferré, B., Platt, S. M., Silyakova, A., Hermansen, O., Allen, G., Pisso, I., Schmidbauer, N., Stohl, A. & Pitt, J. 2016. Extensive release of methane from Arctic seabed west of Svalbard during summer 2014 does not influence the atmosphere. *Geophysical Research Letters*, 43(9), pp. 4624-4631. doi: 10.1002/2016GL068999.

Reagan Matthew, T., Moridis George, J., Elliott Scott, M. & Maltrud, M. 2011. Contribution of oceanic gas hydrate dissociation to the formation of Arctic Ocean methane plumes. *Journal of Geophysical Research: Oceans*, 116(C9). doi: 10.1029/2011JC007189.

Reeburgh, W. S. 2007. Oceanic Methane Biogeochemistry. *Chemical Reviews*, 107(2), pp. 486-513. doi: 10.1021/cr050362v.

Ruppel, C. D. & Kessler, J. D. 2016. The Interaction of Climate Change and Methane Hydrates. *Reviews of Geophysics*. doi: 10.1002/2016RG000534.

Sahling, H., Römer, M., Pape, T., Bergès, B., dos Santos Fereirra, C., Boelmann, J., Geprägs, P., Tomczyk, M., Nowald, N. & Dimmler, W. 2014. Gas emissions at the continental margin west of Svalbard: mapping, sampling, and quantification. *Biogeosciences*, 11(21), pp. 6029-6046. doi: 10.5194/bg-11-6029-2014.

Saloranta, T. M. & Svendsen, H. 2001. Across the Arctic front west of Spitsbergen: high-resolution CTD sections from 1998–2000. *Polar Research*, 20(2), pp. 177-184. doi: 10.3402/polar.v20i2.6515.

Schauer, U., Fahrbach, E., Osterhus, S. & Rohardt, G. 2004. Arctic warming through the Fram Strait: Oceanic heat transport from 3 years of measurements. *Journal of Geophysical Research: Oceans*, 109(C6). doi: 10.1029/2003JC001823.

Shakhova, N., Semiletov, I., Leifer, I., Sergienko, V., Salyuk, A., Kosmach, D., Chernykh, D., Stubbs, C., Nicolsky, D., Tumskoy, V. & Gustafsson, O. 2014. Ebullition and storm-induced methane release from the East Siberian Arctic Shelf. *Nature Geosci*, 7(1), pp. 64-70. doi: 10.1038/ngeo2007.

Shakhova, N., Semiletov, I., Salyuk, A., Yusupov, V., Kosmach, D. & Gustafsson, Ö. 2010. Extensive Methane Venting to the Atmosphere from Sediments of the East Siberian Arctic Shelf. *Science*, 327(5970), pp. 1246-1250. doi: 10.1126/science.1182221.

Skogseth, R., Haugan, P. M. & Jakobsson, M. 2005. Watermass transformations in Storfjorden. *Continental Shelf Research*, 25(5), pp. 667-695. doi: 10.1016/j.csr.2004.10.005.

Sundermeyer, M. A. & Ledwell, J. R. 2001. Lateral dispersion over the continental shelf: Analysis of dye release experiments. *Journal of Geophysical Research: Oceans*, 106(C5), pp. 9603-9621. doi: 10.1029/2000JC900138.

Tishchenko, P., Hensen, C., Wallmann, K. & Wong, C. S. 2005. Calculation of the stability and solubility of methane hydrate in seawater. *Chemical geology*, 219(1), pp. 37-52. doi: 10.1016/j.chemgeo.2005.02.008.

Veloso, M., Greinert, J., Mienert, J. & De Batist, M. 2015. A new methodology for quantifying bubble flow rates in deep water using splitbeam echosounders: Examples from the Arctic offshore NW‐Svalbard. *Limnology and Oceanography: Methods*, 13(6), pp. 267-287. doi: 10.1002/lom3.10024.

Weber, T. C., Mayer, L., Jerram, K., Beaudoin, J., Rzhanov, Y. & Lovalvo, D. 2014. Acoustic estimates of methane gas flux from the seabed in a 6000 km2 region in the Northern Gulf of Mexico. *Geochemistry, Geophysics, Geosystems*, 15(5), pp. 1911-1925. doi: 10.1002/2014GC005271.

Westbrook, G. K., Thatcher, K. E., Rohling, E. J., Piotrowski, A. M., Pälike, H., Osborne, A. H., Nisbet, E. G., Minshull, T. A., Lanoisellé, M. & James, R. H. 2009. Escape of methane gas from the seabed along the West Spitsbergen continental margin. *Geophysical Research Letters*, 36(15). doi: 10.1029/2009GL039191.

Wiesenburg, D. A. & Guinasso Jr, N. L. 1979. Equilibrium solubilities of methane, carbon monoxide, and hydrogen in water and sea water. *Journal of Chemical and Engineering Data*, 24(4), pp. 356-360. doi: 10.1021/je60083a006.